**PAPER**

# Interfacial oxygen-octahedral-tilting-driven electrically tunable topological Hall effect in ultrathin SrRuO$_3$ films

To cite this article: Youdi Gu *et al* 2019 *J. Phys. D: Appl. Phys.* **52** 404001

View the article online for updates and enhancements.

Recent citations

# IOP ebooks™

Bringing you innovative digital publishing with leading voices to create your essential collection of books in STEM research.

Start exploring the collection - download the first chapter of every title for free.

# Interfacial oxygen-octahedral-tilting-driven electrically tunable topological Hall effect in ultrathin SrRuO₃ films

**Youdi Gu**[1,2,10]**, Yi-Wen Wei**[3,10]**, Kun Xu**[4,5,10]**, Hongrui Zhang**[6]**,
Fei Wang**[1,7]**, Fan Li**[2]**, Muhammad Shahrukh Saleem**[2]**, Cui-Zu Chang**[7]**,
Jirong Sun**[6]**, Cheng Song**[2,11]**, Ji Feng**[3,8,9,11]**, Xiaoyan Zhong**[4,11]**,
Wei Liu**[1]**, Zhidong Zhang**[1]**, Jing Zhu**[4]** and Feng Pan**[2]

[1] Shenyang National Laboratory for Materials Science, Institute of Metal Research, University of Chinese Academy of Sciences, Chinese Academy of Sciences, Shenyang 110016, People's Republic of China
[2] Key Laboratory of Advanced Materials (MOE), School of Materials Science and Engineering, Tsinghua University, Beijing 100084, People's Republic of China
[3] International Center for Quantum Materials, School of Physics, Peking University, Beijing 100871, People's Republic of China
[4] National Center for Electron Microscopy in Beijing, Key Laboratory of Advanced Materials (MOE), The State Key Laboratory of New Ceramics and Fine Processing, School of Materials Science and Engineering, Tsinghua University, Beijing 100084, People's Republic of China
[5] Central Nano and Micro Mechanism, Beijing, Tsinghua University, Beijing 100084, People's Republic of China
[6] Beijing National Laboratory for Condensed Matter Physics, Institute of Physics, University of Chinese Academy of Sciences, Chinese Academy of Sciences, Beijing 100190, People's Republic of China
[7] Department of Physics, Pennsylvania State University, University Park, PA 16802, United States of America
[8] Collaborative Innovation Center of Quantum Matter, Beijing 100871, People's Republic of China
[9] CAS Center for Excellence in Topological Quantum Computation, University of Chinese Academy of Sciences, Beijing 100190, People's Republic of China

E-mail: songcheng@mail.tsinghua.edu.cn (C Song), jfeng11@pku.edu.cn (J Feng) and xyzhong@mail.tsinghua.edu.cn (X Zhong)

CrossMark

## Abstract

Topological spin textures as an emerging class of topological matter offer a medium for information storage and processing. The recently discovered topological Hall effect (THE) is considered as a fingerprint for electrically probing the Dzyaloshinskii–Moriya (DM) interaction and corresponding non-trivial spin-textures. In this paper, the THE and its electrical control are observed in ultrathin ($\leqslant 8$ unit cells. u.c.) 4D ferromagnetic SrRuO₃ films grown on SrTiO₃(0 0 1) substrates, indicating the existence of gate-bias-tunable DM interaction in the single SrRuO₃ layer without contacting 5D oxide SrIrO₃ layer. High-resolution lattice structure analysis revealed that the interfacial RuO₆ octahedral tilting induced by local orthorhombic-to-tetragonal structural phase transition exists across the SrRuO₃/SrTiO₃ interface, which naturally breaks the inversion symmetry. Our theoretical calculations demonstrate that the DM interaction arises owing to the broken inversion symmetry and strong spin–orbit interaction of 4D SrRuO₃. This interfacial RuO₆ octahedral tilting-induced DM interaction can stabilize the Néel-type magnetic skyrmions, which in turn accounts for the observed THE in transport. Besides the fundamental significance, the understanding of THE in

[10] These authors contributed equally to this work.
[11] Author to whom any correspondence should be addressed.

oxides and its electrical manipulation presented in this work could advance the low power cost topological electronic and spintronic applications.

S Supplementary material for this article is available online

(Some figures may appear in colour only in the online journal)

## 1. Introduction

Topologically nontrivial spin textures have attracted extensive attention since they harbor elegant physics associated with the real space Berry curvature [1–3], and novel quantum transport phenomena and hold potential for energy efficient spintronic applications [4–6]. One intriguing example is the skyrmion spin texture, a topologically protected vortex-like object with swirling spin configuration. The magnetic skyrmion has been observed in B20 metallic magnets [7–9], interfacial asymmetric magnetic multilayers [10, 11], and ferromagnetic oxide films, such as (La,Sr)MnO$_3$ [12], SrRuO$_3$/SrIrO$_3$ heterostructures [13–15] and SrRuO$_3$/BaTiO$_3$ heterostructures [16]. When an electrical current flows through a skyrmion texture, the electron spin couples adiabatically with the skyrmion spin and experiences a fictitious magnetic field (i.e. Berry curvature) in real space. This field can generate an additional Hall conductance, which is a novel quantum phenomenon referred to as topological Hall effect (THE) [17, 18]. The presence of THE is considered as an electrical transport signature of the skyrmion spin textures [5, 13–19].

The formation of skyrmion in a thin film system needs the non-collinear Dzyaloshinskii–Moriya (DM) interaction expressed as $H_{DM} = \sum_{i,j} \boldsymbol{D}_{ij} \cdot (\boldsymbol{S}_i \times \boldsymbol{S}_j)$ [11, 20, 21], where the $\boldsymbol{D}_{ij}$ is the DM vector that determines the strength and sign of the DM interaction between a pair of spins $\boldsymbol{S}_i$ and $\boldsymbol{S}_j$. The DM interaction can be realized in a thin film system if the following two conditions are satisfied: (i) broken inversion symmetry, (ii) strong spin–orbit coupling (SOC). For example, the DM interaction can be generated in heavy metal/ferromagnet/oxide sandwiches [11, 22], where the two interfaces and the heavy metal contribute to the broken inversion symmetry and SOC, respectively. Experimentally, a combination of the strong SOC of the ferromagnetic layer (e.g. CrTe and Mn-doped Bi$_2$Te$_3$) and broken interfacial inversion symmetry for single-layered CrTe [23] and Mn-doped Bi$_2$Te$_3$ [24] thin films grown on SrTiO$_3$(1 1 1) substrates can also give rise to substantial DM interaction and concomitant THE. Recently, THE was observed in SrRuO$_3$/SrIrO$_3$ bilayers [13–15] and was explained by the formation of DM interaction stemming from the strong SOC of 5D SrIrO$_3$ and broken inversion symmetry. Further work on SrRuO$_3$ films interfaced to ferroelectric BaTiO$_3$ films with off-centering Ru-Site distortions yielded similar THE signatures [16]. A natural and important question is whether there is a simplified approach to magnetic skyrmion and THE in SrRuO$_3$ thin film without the assistance of 5D elements or ferroelectric layer, especially since SOC

is already strong in Ru. Very recently, Qin *et al* [25] reported the emergence of THE in oxygen-deficient epitaxial SrRuO$_3$ films grown at lower oxygen pressure of 20 mTorr and attributed to the DM interaction arising from the inversion asymmetry at the naturally occurring surface region of the SrRuO$_3$ films (the interface of the film top surface with its environment). However, since SrRuO$_3$ shows intricate oxygen octahedral structures relying on the deposition oxygen pressure and thickness [26, 27], some intrinsic local structural deformations within oxide/substrate interface region caused by symmetry mismatch are easy to occur and lead to inversion asymmetry [27, 28], thus can significantly affect electronic and magnetic properties of SrRuO$_3$ films. So it is still an open question for the origin of THE in ultrathin SrRuO$_3$ system. Considering that the THE is usually attributed to the interface-driven quantum transport phenomenon, it would be important to investigate how the local deformation, accompanied by the octahedral tilt and rotation near the SrTiO$_3$/SrRuO$_3$ interface region, can affect the structural and transport properties of ultrathin SRO films on STO substrates.

Octahedral distortions such as deformation and tilting (or rotation) in oxides are currently of great interest, which provides broad opportunities for modulating physical properties of the oxide films, such as magnetic anisotropy, conductivity and exchange coupling [29–33]. The octahedral distortions can naturally break the inversion symmetry, thus provide a potential way to generate skyrmion spin texture. SrRuO$_3$, a rare example of 4D band metal with a pseudo-cubic perovskite crystal structure, is a well-known itinerant ferromagnet with a Curie temperature ($T_C$) of ~160 K [34]. A number of intriguing electromagnetic phenomena have been demonstrated to be closely related to the Berry curvature in SrRuO$_3$, including magnetic monopoles [35], Weyl fermions [36], and even quantum anomalous Hall state [37]. These results indicate that the 4D metallic ferromagnet SrRuO$_3$ should possess considerable spin–orbit interaction, as anticipated. Considering the broken inversion symmetry induced by octahedral tilting in the SrRuO$_3$ films, a non-vanishing DM interaction and resultant THE are highly expected in single-layered SrRuO$_3$ films. Moreover, since electric-field control of interfacial magnetism is of special interest for high-density and low-power consumption information storage [38], it is of great importance for electronic and spintronic applications to achieve an electrically tunable DM interaction. However, works that utilize an electric-field to effectively manipulate the DM interaction are scarce for oxide heterostructures. Although the electric-field-induced variation of DM interaction was recently reported for

J. Phys. D: Appl. Phys. **52** (2019) 404001

Y Gu *et al*

SrRuO$_3$/SrIrO$_3$ interface [14], the role of the electric-field for DM interaction variation has yet to be clarified. Because of the short screening length of the electric-field in itinerant ferromagnet SrRuO$_3$, we expect that an electric-field applied to the ultrathin SrRuO$_3$/SrTiO$_3$ heterostructures may be utilized to efficiently manipulate the DM interaction due to the presence of additional Rashba effect [39, 40], resulting in more interesting physical behaviors. In the investigation described below, the THE and its electrical control are observed for ultrathin SrRuO$_3$ single-layered films grown on SrTiO$_3$(0 0 1) substrates. In these samples, a peculiar pattern of oxygen octahedral tilting is observed by high-resolution lattice structure analysis, which adds to the inversion asymmetry in the SrRuO$_3$ layers right next to the SrTiO$_3$. The ensuing enhancement of the DM interaction is shown to stabilize the Néel-type magnetic skyrmion spin configuration, leading to THE-type transport. In addition, the interfacial oxygen octahedral tilting can be suppressed and/or blocked by inserting a few BaTiO$_3$ layers between SrTiO$_3$ and SrRuO$_3$, resulting in the absence of inversion symmetry breaking and disappearence of THE. The present work opens a unique and promising window for the design of artificial materials with electrically tunable topological spin textures and the associated quantum transport properties.

## 2. Experimental

High-quality SrTiO$_3$/SrRuO$_3$ and SrTiO$_3$/BaTiO$_3$/SrRuO$_3$ heterostructures were grown by pulsed laser deposition (PLD) with a KrF excimer laser from stoichiometric SrRuO$_3$ and BaTiO$_3$ targets in layer-by-layer mode on the (0 0 1)-oriented SrTiO$_3$ substrates (5 mm × 5 mm × 0.5 mm). The SrRuO$_3$ was grown at 700 °C with an oxygen background pressure of 100 mTorr and a repetition rate of 5 Hz, while BaTiO$_3$ was grown at 720 °C with an oxygen background pressure of 4 mTorr and a repetition rate of 2 Hz. The growth was *in situ* monitored by reflection high-energy electron diffraction (RHEED). This allows precise control of the film thickness at the unit cell scale and accurate characterization of the growth dynamics. After growth process, the samples were slowly cooled down to room temperature in 300 Torr of oxygen pressure at a rate of ~5 °C min$^{-1}$ to improve the oxidation level.

The x-ray reciprocal space mappings (RSMs) of the films were measured by using a Bruker x-ray diffractometer equipped with thin film accessories (D8 Discover, Cu K$_\alpha$ radiation) at the Beijing National Laboratory for Condensed Matter Physics, Institute of Physics, Chinese Academy of Sciences.

A superconducting quantum interference device (SQUID) magnetometer with a magnetic field applied perpendicular to the film plane was used to measure the magnetic properties of samples because the magnetic easy axis of the SrRuO$_3$ film is nearly perpendicular to the film plane when grown on SrTiO$_3$(0 0 1) substrate. Low temperature magneto-optic Kerr effect (MOKE) was measured with a laser at 720 nm in polar geometry by applying external magnetic field perpendicular to samples. A Hall-bar geometry device was used to carry out the electrical transport measurements in a 9 Tesla

mini Cryogen-Free Measurement System for Precision Measurement of Physical Properties (CFMS-9, Cryogenic Limited, United Kingdom). The sample was patterned into a Hall-bar by photolithography and Ar ion etching process for Hall and longitudinal resistivity measurements. The effective channel is 400 $\mu$m long and 100 $\mu$m wide. All Ti (20 nm)/Au (80 nm) electrodes were deposited using electron-beam evaporation, resulting in low-resistant Ohmic contacts. Magnetic field dependence of Hall resistivity was obtained by subtracting the ordinary Hall contribution by linear extrapolation in the high magnetic field region. Antisymmetric process was performed for all the Hall data shown in this paper.

The cross-section TEM lamellas of the SrTiO$_3$/SrRuO$_3$ and SrTiO$_3$/BaTiO$_3$/SrRuO$_3$ epitaxial thin films along the desired zone axes were prepared by using a Zeiss dual-beam focused ion beam (FIB). The thin films were capped with a thin Pt film to prevent from being damaged during sample preparation of TEM cross-section specimen. The final thinning step was performed with 2 kV 1 mA Ar ion milling to remove the amorphous layer. STEM analysis was performed on a double aberration-corrected microscope FEI Titan G3 electron microscope equipped with an aberration corrector for the probe-forming lens and a high-brightness gun, as well as a super-EDX 4-quadrant detector, operated at 300 kV acceleration voltage to acquire high-angle annular dark field (HAADF)-STEM and annular bright-field (ABF)-STEM images and conduct the EDX experiment. The setup for STEM convergence semi-angle used was 25 mrad, providing a probe size of ~0.6 Å. The collection semi-angle from 70–160 mrad and 11–29 mrad for HAADF and ABF imaging, respectively. Dual electron energy loss spectroscopy (EELS) mode is used to simultaneously acquire both the zero-loss and core-loss EELS spectra to ensure intrinsic chemical shift compensated the instrument drift by the correction of zero-loss. And atomic scale line scan of EELS spectra across the interface is acquired with a higher energy dispersion (0.1 eV/channel) to obtain Ti $L_{2,3}$- and O $K$-edge EELS.

## 3. Results and discussion

High-quality SrRuO$_3$ epitaxial films with various thicknesses (4–50-unit cells, u.c.) were grown on insulating SrTiO$_3$(0 0 1) substrates using PLD (see figure S1 in supplementary data (stacks.iop.org/JPhysD/52/404001/mmedia) and Experimental). Films were then patterned into Hall bar geometry devices for transport measurements with an applied current of 5 $\mu$A. An actual Hall bar device showing the transport measurement configurations was presented in figure S2 in supplementary data. The longitudinal resistivity ($\rho_{xx}$) versus temperature ($T$) curves of the SrRuO$_3$ films were measured from room temperature to 5 K. As the film thickness decreases, $\rho_{xx}$ continuously increases and three different regimes can be identified. For the thickness of 15–50 u.c., the films show a metallic behavior over the entire temperature range of 5–300 K. However, the $\rho_{xx}$ of films undergoes a metal-insulator-transition when the thickness $t$ is less than 10 u.c. Samples with a thickness of 4 u.c. or less display an insulating behavior in the entire temperature regime (see figure S3 in supplementary
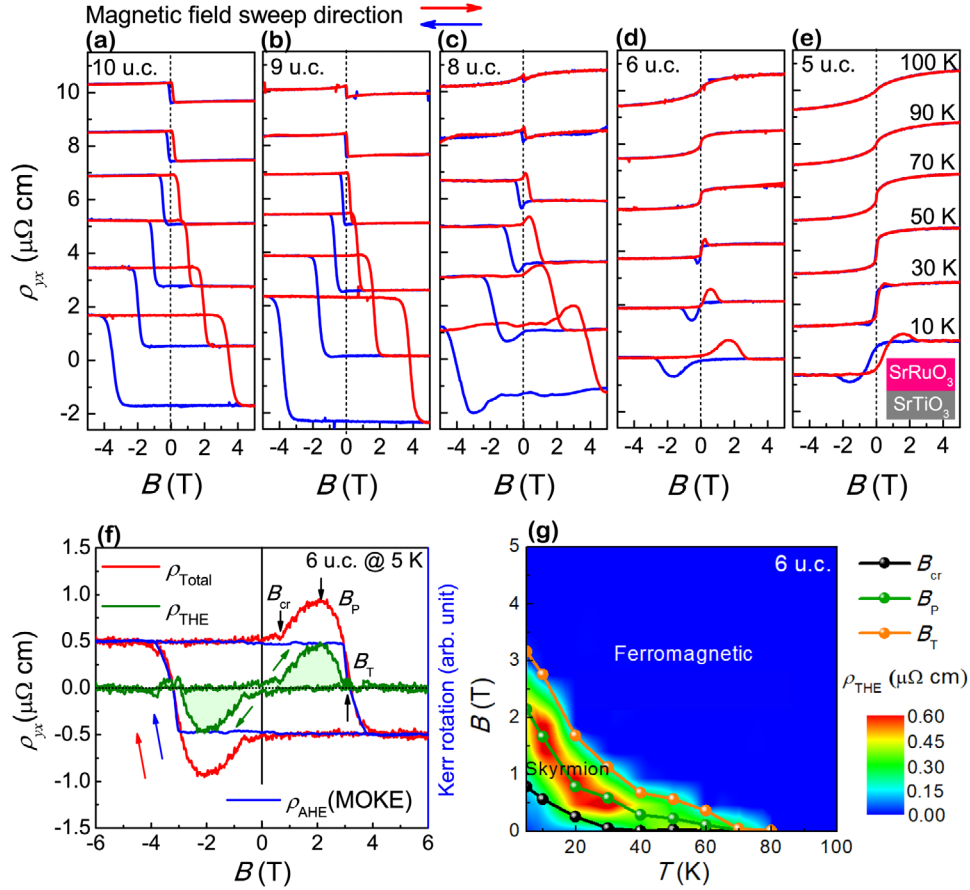
**Figure 1.** THE in SrRuO$_3$ single-layered films. (a)–(e) $\rho_{yx}$-$B$ curves of single-layered SrRuO$_3$ films with various film thicknesses, $t = 10$ u.c. (a), 9 u.c. (b), 8 u.c. (c), 6 u.c. (d) and 5 u.c. (e) in the temperature range of 10–100 K. The red (blue) curve represents the ascending (descending) branch. The graphs have been shifted along the vertical axes for clarity. (f) Representative magnetic field dependence of topological Hall resistivity $\rho_{THE}$ at 5 K of 6 u.c. SrRuO$_3$ film extracted from $\rho_{total}$ and $\rho_{AHE}$ (MOKE) curves. (g) The contour mapping of extracted $\rho_{THE}$ of 6 u.c. SrRuO$_3$ film as a function of external magnetic field ($B$) and temperature ($T$). The hump area between the $B_{cr}$ (field for the appearance of THE) and $B_T$ (field for the disappearance of THE) lines represents the skyrmion regime. THE reaches its maximum value at the field of $B_P$.

data) [41–43]. We show in figures 1(a)–(d) the magnetic field ($B$) dependent transverse Hall resistivity ($\rho_{yx}$) of the ultrathin SrRuO$_3$ films (10, 9, 8, 6 and 5 u.c.). Note that the ordinary Hall contribution determined by the linear extrapolation in the high magnetic field region has been subtracted. For the 10 u.c.-thick SrRuO$_3$ sample (figure 1(a)), the $\rho_{yx}$-$B$ curve exhibits the typical anomalous Hall effect (AHE) signature in the temperature range of 10–100 K, indicating the perpendicular magnetic anisotropy of the SrRuO$_3$ film (see figure S4 in supplementary data) [34]. The Curie temperature ($T_C$) of 10 u.c. SrRuO$_3$ is ~138 K (see figure S3 in supplementary data). A comparable AHE signal is also observed for the 9 u.c.-thick film (figure 1(b)), in which the ferromagnetic ordering at fixed temperature is a bit weaker than that of 10 u.c. sample because of the lower $T_C$ (see figure S3 in supplementary data).

The situation changes dramatically when the film thickness is reduced to 8 u.c. (figure 1(c)). In stark contrast to conventional AHE of ferromagnetic conductors, the Hall traces exhibit a clear anomaly characterized by the appearance of a hump or dip structure superimposing on the usual AHE loop while scanning the field between −5 and 5 T. Similar features are also observed in the 6 and 5 u.c.-thick samples (figures

1(d) and (e)) when the temperature is below 70 K (closed to the $T_C$s). The $T_C$ of 6 u.c. sample is ~105 K. The 5 u.c. sample has an even lower $T_C$ (~95 K) (see figure S3 in supplementary data). The existence of hump/dip structure only in thinner films implies the driven force should be closed to the interface. The hump/dip structure is the typical feature of the THE [13–16, 19, 23–25], which has a fundamentally different origin from AHE. It is proposed that a real space geometric phase acts on an electron as an emergent effective electromagnetic field through the interaction with the topological skyrmion spin textures [18]. Consequently, the moving electrons are scattered by the topological skyrmion spin textures in a direction opposite to the scenario of AHE, thus generating a topological Hall voltage [18, 19]. THE has been recently observed in interfacial magnetic skyrmion systems as exemplified by Cr$_x$(Bi$_{1-y}$Sb$_y$)$_{2-x}$Te$_3$/(Bi$_{1-y}$Sb$_y$)$_2$Te$_3$ interface [19], SrRuO$_3$/SrIrO$_3$ interface [13–16], CrTe/SrTiO$_3$ interface [23], Mn-doped Bi$_2$Te$_3$/SrTiO$_3$ system [24] and SrRuO$_3$/BaTiO$_3$ interface [16]. The present work provides the clear evidence for the THE in single-layered SrRuO$_3$ films (below 8 u.c.) grown on SrTiO$_3$(0 0 1) substrates, which is similar to recently reported results [25]. Differently, the thickness range

J. Phys. D: Appl. Phys. **52** (2019) 404001

Y Gu *et al*

is 3–10 nm for THE to appear in [25]. Note that the different thickness range for the THE to appear may be related to different growth conditions (e.g. oxygen pressure and growth temperature).

Phenomenologically, the total Hall resistivity can be thought of as having three components [13, 14]: the ordinary Hall effect, the AHE and the THE, expressed as

$$\rho_{yx} = R_0 B + R_S M + \rho_{THE}, \tag{1}$$

where $R_0$ is the ordinary Hall coefficient, $R_S$ is the anomalous Hall coefficient, $\rho_{THE}$ is the topological Hall resistivity arising from topological skyrmion spin textures, and $B$ is the magnetic field perpendicular to the film plane. Compared with other four samples (figures 1(a)–(d)), the magnetization $M$ of 5 u.c.-thick film is lower but still sizable (see figure S5 in supplementary data), and the sign of its AHE curves totally becomes positive (figure 1(e)) from 10 to 100 K, indicating the singularity of the band structure of SrRuO$_3$. This is possibly due to reduced $M$ [34, 43, 44].

To have a close inspection of THE, we solely extract the THE contribution from total Hall curves by measuring low temperature magneto-optical Kerr effect (MOKE) data for the representative 6 u.c. SrRuO$_3$ film. Note that it is very hard to discern magnetic signal contribution of ultrathin SrRuO$_3$ films from hysteresis loop measurements due to the large diamagnetic background signal of SrTiO$_3$ substrates [13, 42]. Thus, the magnetic properties of films are determined from MOKE measurements, which are only sensitive to the out-of-plane component of magnetization [42]. The representative magnetic field dependence of topological Hall resistivity $\rho_{THE}$ (olive curve) at 5 K of 6 u.c. SrRuO$_3$ film extracted from total Hall resistivity $\rho_{total}$ (red curve) and MOKE (blue curve) data is plotted in figure 1(f). From the established quite fine fitting, it is thus demonstrated that we can indeed obtain the $\rho_{THE}$ (hump/dip area) by subtracting $\rho_{AHE}$ from the total Hall resistivity $\rho_{total}$. Considering the ascending branch with magnetic field from 0 to 6 T, $\rho_{THE}$ curve deviates from the zero topological Hall electricity at the critical field $B_{cr}$ of ~0.86 T and develops into a broad hump and reaches a peak of $\rho_{THE} \approx 0.5 \mu\Omega$ cm at a specific field $B_P$ of ~2.14 T. Above a characteristic field $B_T$ of ~3.16 T, the $\rho_{THE}$ curve decreases to zero. This $\rho_{THE}$-$B$ behaviour suggests that the topological spin structures with scalar spin chirality are induced when the ferromagnetic spins begin to be reserved in SrRuO$_3$.

Based on the extracted THE from all the Hall traces at different temperatures, we build a skyrmion phase diagram for 6 u.c. SrRuO$_3$ sample, as represented by contour mapping of derived $\rho_{THE}$ value in the temperature $T$ and magnetic field $B$ planes, as displayed in figure 1(g). The skyrmion phase indicated by the emergence of THE extends across a wide region in the $T$–$B$ plane, forming in a wide temperature range up to 80 K and occupying almost all the region below $B_T$ even including the zero magnetic field ($B_{cr}$ of 0 T). Within such a broad temperature and magnetic field ranges, the sign of $\rho_{THE}$ is always positive and varies systematically, irrespective of sign reversal of AHE at ~30 K. The observed positive THE suggests that it indeed has a totally different origin from AHE. The topology of the phase diagram here is similar to those

obtained recently in the SrRuO$_3$/SrIrO$_3$ and SrRuO$_3$/BaTiO$_3$ bilayer systems [13, 14, 16]. In a skyrmion system, each skyrmion traps an effective magnetic flux quantum $\phi_0 = h/e$, where $h$ is the Planck constant, $e$ is the elementary charge. The topological Hall resistivity induced by the skyrmion [13, 14] can be written as

$$\rho_{THE} \approx PR_0 B^z_{eff} = PR_0 n_{sk}\phi_0, \tag{2}$$

where $B^z_{eff} = n_{sk}\phi_0$ is the fictitious effective field, $P$ denotes the spin polarization of the conduction electron in SrRuO$_3$ and $n_{sk}$ is skyrmion density. Adopting the value of $R_0 = -0.10 \mu\Omega$ cm T$^{-1}$ measured at $T = 5$ K and the $P$ in the range from $-9.5\%$ to $-50\%$ [45, 46], the skyrmion density $n_{sk}$ estimated from equation (2) varies from ~$2.5 \times 10^{15}$ to ~$1.3 \times 10^{16}$ m$^{-2}$. Consequently, the estimated length scale of one single skyrmion is $n_{sk}^{-1/2}$ ~ 9–20 nm. These values are quite reasonable compared with the typical diameter of DM interaction-induced skyrmion, which ranges from 5 to 100 nm [18, 24].

An interesting issue is the manipulation of the THE. To further investigate the nature of the THE, we choose the 5 u.c. SrRuO$_3$ sample by applying a gate voltage ($V_g$) to see its effect on THE. The inset of figure 2(a) presents the schematic of the bottom gate dependence of measurements at 5 K. Because of the huge dielectric constant ($\varepsilon$ ~ 23 000) [47] of SrTiO$_3$ at low temperatures, an electrode of dried silver conductive paint on the bottom side of the SrTiO$_3$ substrate can form a field-effect transistor, which can be used to tune the chemical potential of the SrRuO$_3$ films. Figure 2(a) shows $V_g$ dependence of longitudinal resistivity $\rho_{xx}$. The variation of $\rho_{xx}$ ($\Delta\rho_{xx}/\rho_{xx} = ([\rho_{xx}(V_g) - \rho_{xx}(0)]/\rho_{xx}(0))$ is $-3.2\%$ (electron accumulation) under $V_g = 200$ V and $3.5\%$ (electron depletion) under $V_g = -170$ V. It implies small or even negligible changes in carrier density (figure 2(c)), possibly due to the large carrier density of the intrinsic SrRuO$_3$ film [14, 48].

In contrast to $\rho_{xx}$, the $V_g$ has a much stronger effect on AHE and THE. Figure 2(b) shows $\rho_H$–$B$ curves under the typical gate biases of $-170$, $-100$, 0, 100, and 200 V, where the ordinary Hall effect was not subtracted. Although the overall change of the slope (the ordinary Hall effect) at different $V_g$ is not so pronounced (coincide with the results in figure 2(a)), the AHE and THE parts are modulated within a large scale, as highlighted in figure 2(d). The variation of AHE ($\Delta\rho_{yx}^0/\rho_{yx}^0 = [\rho_{yx}^0(V_g) - \rho_{yx}^0(0)]/\rho_{yx}^0(0)$) is 100% for $V_g = 200$ V and $-34.5\%$ for $V_g = -170$ V, which is at least one order of magnitude larger than the change of $\rho_{xx}$. Here $\rho_{yx}^0$ represents the zero magnetic field Hall resistivity.

Meanwhile, the THE (indicated by shaded area) exists under all electric biases but is most pronounced under $V_g = -170$ V and greatly suppressed under $V_g = 200$ V. We emphasize that, it is technically challenging to directly measure the *in situ* MOKE or hysteresis loop data due to the volatile bottom electric field in our case. The THE is roughly separated by subtracting the AHE signal through linear fitting of the high magnetic field data, since the shaded area is almost same to the $\rho_{THE}$ according to the established fine subtraction in figure 1(f). The critical fields and the values of $\rho_{THE}$ are summarized in
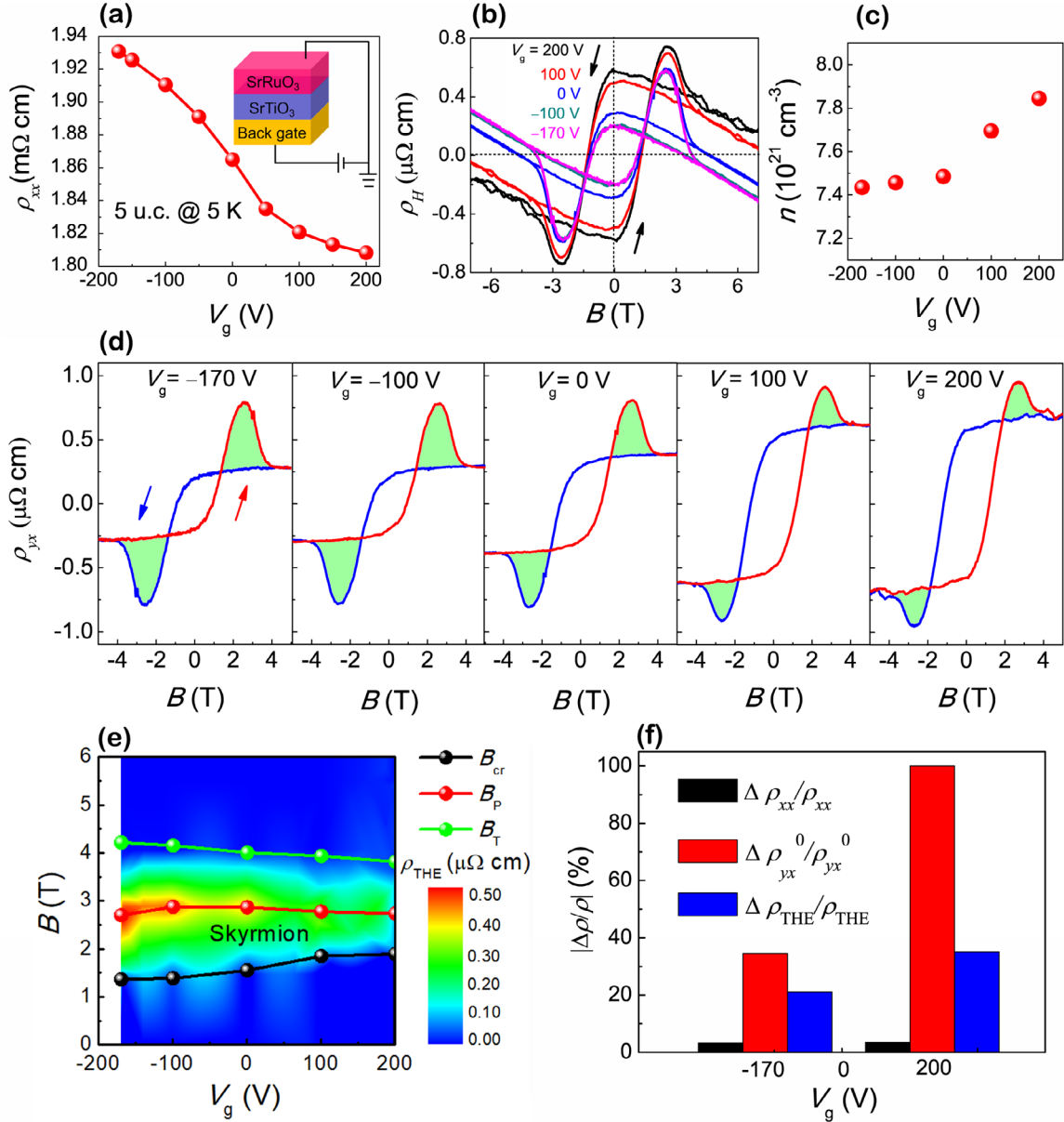
**Figure 2.** Electric-field control of THE. (a) Gate voltage $V_g$ dependence of the longitudinal resistivity $\rho_{xx}$ of 5 u.c. SrRuO$_3$ films at 5 K. Inset: the schematic of bottom gate dependence of transport measurements using the SrTiO$_3$ as the dielectric layer. (b) Magnetic field dependence of Hall resistivity $\rho_H$ (original data with the ordinary Hall effect) of 5 u.c. SrRuO$_3$ films at 5 K for $V_g = -170, -100, 0, 10$, and 200 V. (c) Carrier density $n$ plotted as a function of the gate voltage $V_g$. (d) $V_g$ dependence of $\rho_{yx}$-B curves after subtracting the ordinary Hall effect. (e) Contour mapping of $\rho_{THE}$ in the $B$–$V_g$ plane at 5 K for 5 u.c.-thick SrRuO$_3$ films. The broad area between the $B_{cr}$ and $B_T$ lines represents the skyrmion regime in the whole $V_g$ ranges. THE reaches its maximum value at the field of $B_P$. (f) The absolute value of electrical resistivity variation ($|\Delta\rho/\rho|$) based on two typical $V_g$s of $-170$ and 200 V.

the $V_g$–$B$ plane (figure 2(e)). The broad shaded area between the $B_{cr}$- and $B_T$–$V_g$ lines represents the skyrmion phase. The peak values of $\rho_{THE}$ are 0.52, 0.43, and 0.28 $\mu\Omega$ cm under $V_g = -170, 0$, and 200 V, respectively. The corresponding variation in peak of $\rho_{THE}$ ($\Delta\rho_{THE}/\rho_{THE} = [\rho_{THE}(V_g) - \rho_{THE}(0)]/\rho_{THE}(0)$) is 21% under $V_g = -170$ V and $-35\%$ under $V_g = 200$ V. As a consequence, the length scale of individual topological skyrmion spin texture, estimated from equation (2), is ~8 nm ($V_g = -170$ V) and ~10.5 nm ($V_g = 200$ V) adopting the spin polarization of $P = -9.5\%$ [45]. The length scale of the one single skyrmion scatters in the range of 10–30 nm when $P$ varies from $-20\%$ to $-50\%$

[13, 46]. Therefore, the THE in the single-layered SrRuO$_3$ is robust, occurring in a wide range of temperatures, magnetic fields, and gate voltages.

A comparison of the $V_g$ control of carrier density and AHE/THE in figure 2(f) suggests that the observed large modulation of AHE and THE cannot be simply explained by the $V_g$-induced carrier density change. The detailed qualitative explanations are shown in figure S6 in supplemental data based on [14]. Possibly, the SOC may suffer from the tuning of electric gate, resulting in a variation in DM interaction. We note that the coercive field ($H_C$) of the AHE curves monotonically changes from 1.19 T ($V_g = 200$ V) to 1.07 T ($V_g = 0$),
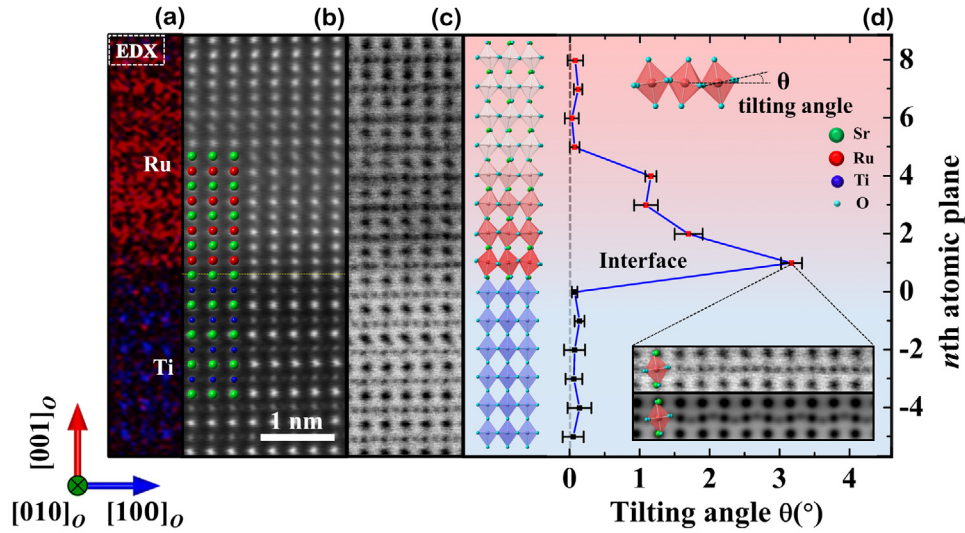
**Figure 3.** Atomic-scale characterization of interfacial $RuO_6$ oxygen octahedral tilting across the $SrRuO_3/SrTiO_3$ interface. (a)–(c) The Ru and Ti elemental mapping (a) HAADF-STEM (b), and ABF-STEM (c) images of 8 u.c. $SrRuO_3$ films on the $SrTiO_3$ substrate demonstrate atomically sharp interface without any element intermixing. The atomic positions of oxygen atoms in (c) clearly reveal the oxygen octahedral tilting along transverse direction at a few $RuO_6$ layers. (d) Statistic analysis of depth-dependent oxygen octahedral tilting angles with monolayer resolution across the $SrRuO_3/SrTiO_3$ interface with the corresponding schematic models. The inset shows the magnified ABF-STEM images of the first $SrRuO_3$ layer at the interface and the simulated ABF-STEM image of orthorhombic-like $SrRuO_3$ under the same experimental conditions.

and then to 0.94 T ($V_g = -170$ V) at 5 K (see figure S7 in supplementary data). Meanwhile, AHE also exhibits a dramatic variation under gate biases. Both phenomena are closely related to SOC thus support the modulation of SOC [14]. Note that a similar modulation of THE and AHE of $SrRuO_3$ single layer by ionic liquid gating is recently achieved at the surface region of $SrRuO_3$ film (top gate configuration), which is attributed to the variation of the inversion symmetry and the SOC at the surface region of the $SrRuO_3$ film induced by the ionic liquid gating bias [25]. We emphasize that it is different with our bottom gate case at $SrTiO_3/SrRuO_3$ interface. Since Qin *et al* [25] obtained the $SrRuO_3$ films at a lower oxygen pressure of 20 mTorr and attributed the origin of DM interaction arising from the inversion asymmetry at the naturally occurring surface region of the film, i.e. the interface of the film top surface with its environment.

The transport experiments have revealed the robust THE and electric modulation of THE in ultrathin $SrRuO_3$ single-layered films. An atomic scale analysis of the interfacial structures is required to reveal the physical origin of THE. The atomic scale elemental mapping and the corresponding HAADF-STEM and ABF-STEM images of the 8 u.c. $SrRuO_3$ films on a $SrTiO_3$ substrate along the $[010]_O$ zone axis of $SrRuO_3$ with an orthorhombic structure are shown in figures 3(a)–(c), respectively. Atomic columns of SrO (green), RuO (red) and TiO (blue) are clearly distinguished from each other based on column intensity differences, clearly revealing a coherent film/substrate interface without any misfit dislocations. The composite color map of Ru atoms in red and Ti atoms in blue shows the atomically sharp interface without any elemental intermixing, which is further confirmed by the absence of peak overlapping between Ti $L_{2,3}$ edges and Ru $M_{2,3}$ edges across the $SrRuO_3/SrTiO_3$ interface, as shown

by the atomic scale EELS (see figure S8 in supplementary data). The O $K$ edges and Ti $L_{2,3}$ edges of eight atomic layers at the interface are almost identical, indicating the same valence states of Ti and the absence of oxygen vacancies. Surprisingly, the oxygen atom positions arranged in a zigzag pattern along transverse direction in a few layers of orthorhombic-like $SrRuO_3$ (O-SRO) at interface are shown in the ABF-STEM image in figure 3(c), demonstrating the interfacial oxygen octahedral tilting of $SrRuO_3$. As shown in the insets of figure 3(d), the magnified ABF-STEM image of the first atomic layer of $SrRuO_3$ at the very interface is consistent with the simulated ABF-STEM image of O-SRO along the $[010]_O$ zone axis under the same experimental conditions. The oxygen octahedral tilting of the $SrRuO_3$ layers close to the interface is smaller than that of bulk orthorhombic $SrRuO_3$ [28, 49], so the layers of $SrRuO_3$ with the oxygen octahedral tilting close to the interface are described as orthorhombic-like structure.

Figure 3(d) shows the variations of oxygen octahedral tilting angles at each atomic layer across the $SrRuO_3/SrTiO_3$ interface by statistical analysis of each RuO and TiO atomic columns. For instance, the average tilting angle of the first atomic layer is about 3.16° with a standard deviation of 0.15°, by analyzing the tilting angles of all the atomic columns (see figure S9 in supplementary data). The oxygen octahedral tilting angle of each atomic plane in $SrRuO_3$ along the $[010]_O$ zone axis dramatically decreases with the increased distance from interface, and there is no oxygen octahedral tilting for the tetragonal $SrRuO_3$ (T-SRO) above the 5th atomic layer. However, the spatial changes of oxygen octahedral tilting here close to the interface region could directly break the inversion symmetry, which contributes to the DM interaction. An epitaxial orientation relationship of $SrTiO_3[110]$

(0 0 1)//O-SRO[0 1 0](0 0 1)//T-SRO[0 1 0](0 0 1) is further confirmed by investigating the samples along $[1 1 0]_O$, $[1 \bar{1} 0]_O$ and $[1 0 0]_O$ zone axes (see figures S8 and S9 in supplementary data). No oxygen octahedral rotation and tilting of T-SRO and O-SRO is observed along these three zone axes, which is consistent with the corresponding project of the perfect crystal (see figures S10 and S11 in supplementary data). Note that the ultrathin SrRuO$_3$ undergoes an orthorhombic-to-tetragonal phase transition. Furthermore, the tetragonality becomes robust with decreasing SrRuO$_3$ film thickness. The intrinsic tetragonal phase is also supported by the x-ray RSMs of 16 u.c. and 8 u.c. SrRuO$_3$ films (see figures S12 and S13 in supplementary data). Our finding coincides with the previously reported results that the tetragonal SrRuO$_3$ phase can be epi-stabilized at room temperature for $t \leqslant 17$ u.c.-thick [27].

In general, the octahedral distortions in ultrathin hybrid structure are expected to accommodate the symmetry-mismatch between the film and substrate with the coherent interface. The corner connectivity of octahedron across the interface drives the film to adopt the tilting symmetry of substrates, which tends to suppress the octahedral tilts (cost energy). Meanwhile, mechanical rigidity of film octahedron tends to develop its own tilting symmetry away from the interface (gain energy) [28, 50, 51]. Consequently, the final rotation and tilting structures of ultrathin hybrid structure are determined by the equilibrium of the energy states between these two competing effects. For the ultrathin SrRuO$_3$ films here, due to the intrinsic robust tetragonal inclination of SrRuO$_3$ itself and the cubic nature of the SrTiO$_3$ substrate, the neighboring interfacial RuO$_6$ octahedra cooperatively adjust their orientation with *c*-axis out-of-plane to follow the growth mode of bottom TiO$_6$ octahedra and connect upper tetragonal RuO$_6$ octahedra (*c*-axis out-of-plane) in such a manner to develop its own $a^- a^- c^+$ tilting symmetry. As an ultimate result there is an octahedral tilting along $[0 1 0]_O$ zone axis but the tilting angle is suppressed to ~3.16°. Afterwards, the orthorhombic RuO$_6$ octahedra with *c*-axis out-of-plane deformation rapidly becomes non-tilting tetragonal symmetry above several unit cell layers. It is then deduced that the pseudo-tetragonal 8 u.c. film is more energetically stable than forming a bulk-like tilting structure. Similar results were observed in ultrathin (La,Sr)MnO$_3$/(LaAlO$_3$)$_{0.3}$(LaSrTaO$_6$)$_{0.7}$ and LaCoO$_3$/SrTiO$_3$ [50, 51].

In addition to the strong SOC readily available in 4D oxide SrRuO$_3$, the other prerequisite for a finite DM interaction is the broken inversion symmetry. This naturally occurs for the asymmetric oxygen octahedron condition between the reconstructed interfacial tilting RuO$_6$ octahedrons and non-tilting RuO$_6$ octahedrons away from the interface induced by the local orthorhombic-to-tetragonal structure phase transition. Thus, the interfacial oxygen octahedral tilting here is highly expected to be responsible for the emergence of THE.

We then turn towards the control experiment of manipulating THE by interfacial engineering. To further confirm the crucial role of the interfacial octahedral tilting on the observed THE, a 2–4 u.c. insulating and nonmagnetic BaTiO$_3$ buffer layer is intentionally inserted between SrRuO$_3$ and SrTiO$_3$ substrates to form SrTiO$_3$/BaTiO$_3$ (*N* u.c.)/SrRuO$_3$

(8 u.c.) heterostructures (*N* = 2, 3, and 4 u.c.) (see figure S1 in supplementary data and Experimental). For the *N* = 2 heterostructure, remarkably, a small, but apparent THE signal (indicated by black arrows) remains at different temperatures from 5 to 70 K (figure 4(a)). The scenario differs dramatically for the heterostructures with *N* = 3 and *N* = 4. Concomitant $\rho_{yx}$–*B* curves at various temperatures are shown respectively in figures 4(b) and (c), where the THE completely disappears. These results suggest that the interfacial RuO$_6$ octahedral tilting is suppressed and/or blocked by the BaTiO$_3$ insertion, resulting in the absence of inversion symmetry breaking. We also observed that the sign of $\rho_{yx}$ is inverted from negative to positive when the BaTiO$_3$ is 3 and 4 u.c.-thick. The sign reversal of AHE is likely due to the singularity in the band structure of SrRuO$_3$ through the Ru–O–Ru bond angle changes [35]. Previous studies reported that the Ru-O-Ru bond angle changes from 168° at the SrRuO$_3$/GdScO$_3$ interface to 180° at the BaTiO$_3$/SrRuO$_3$ interface as the BaTiO$_3$ inserting or capping layer was presented [52]. This would lead to the variation of Berry curvature and resultant band crossings in SrRuO$_3$.

In order to further demonstrate the absence of interfacial octahedral tilting due to the introduction of BaTiO$_3$, the HAADF-STEM and ABF-STEM images of the epitaxial SrTiO$_3$/BaTiO$_3$ (4 u.c.)/SrRuO$_3$ (8 u.c.) thin films were acquired as shown in figures 4(d) and (e), respectively. In comparison with the first SrRuO$_3$ layer at the SrTiO$_3$/SrRuO$_3$ interface, there is no significant octahedral tilting of the first SrRuO$_3$ layer at the BaTiO$_3$/SrRuO$_3$ interface as shown in the figures S9(c) and (d) in supplementary data. Figure 4(f) shows the variations of oxygen octahedral tilting angles at each atomic layer across the SrTiO$_3$/BaTiO$_3$/SrRuO$_3$ interface by statistical analysis, clearly revealing no octahedral tilting in the entire thin films. As is well known, in the periodic table, elements Ba and Sr are in the same family. But the Ba element has a larger atomic radius than Sr. According to the previous investigation [53], the A-site cation size in perovskite oxides acts as an important controlling factor for structural distortions at oxide-based heterointerfaces. Therefore, although both the SrTiO$_3$ and BaTiO$_3$ have the same $a^0 a^0 a^0$ tilting symmetry, the BaTiO$_3$ could suppress the interfacial tilting of SrRuO$_3$ on account of larger A-site cation size.

THE is thought to arise from non-trivial spin textures, especially the topological skyrmions, induced by DM interaction. To clarify the microscopic origin of the experimentally observed THE and its variation under the applied perpendicular electric field in the 5 u.c.-thick SrRuO$_3$ film grown on SrTiO$_3$ substrate, the DM interaction is quantitatively determined based on a tight binding Hamiltonian, and the skyrmion configuration is subsequently obtained (see supplementary data in sections 14–16 for details on calculation). The DM interaction originates from the SOC and spatial inversion symmetry breaking [18, 54]. In our experiment, the inversion symmetry of SrRuO$_3$ film is removed by three factors, namely, the proximity to SrTiO$_3$ substrate, the interfacial oxygen octahedral tilting induced by local orthorhombic-to-tetragonal structural phase transition of SrRuO$_3$ film and, lastly, the applied perpendicular electric field. These three factors are thus expected to contribute to DM interaction, and are described by a tight binding Hamiltonian
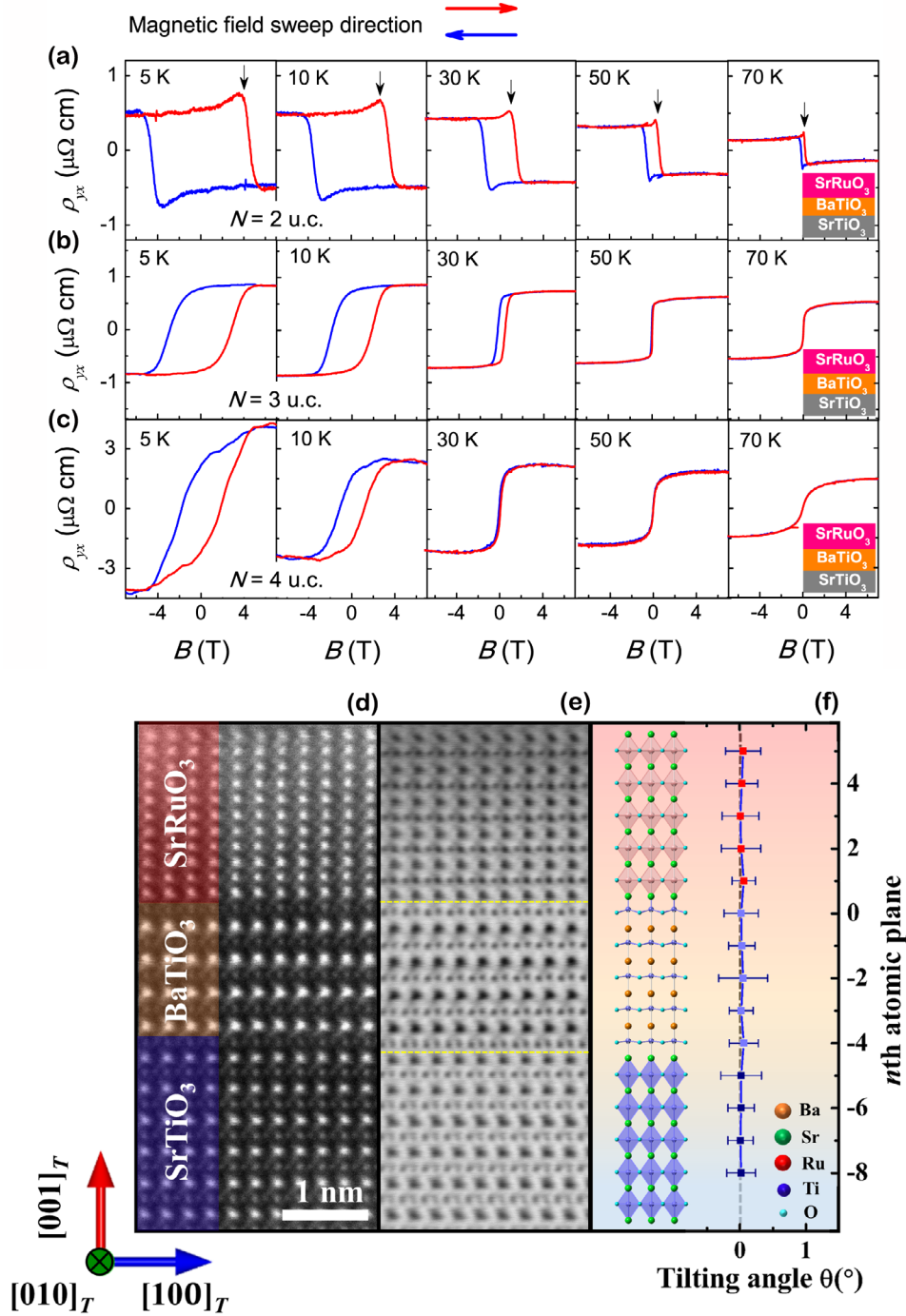
J. Phys. D: Appl. Phys. **52** (2019) 404001

Y Gu *et al*

**Figure 4.** Control of THE via interfacial engineering. (a)–(c) $\rho_{yx}$–$B$ curves of SrTiO$_3$/BaTiO$_3$ ($N$ u.c.)/SrRuO$_3$ (8 u.c.) [$N = 2$ u.c. (a), 3 u.c. (b) and 4 u.c. (c)] ($N$: number of monolayers in BaTiO$_3$ layer) heterostructures at various temperatures. Blue (red) curve represents the process for decreasing (increasing) magnetic field. Ordinary Hall contribution is subtracted by linear extrapolation in the high magnetic field region. (d) and (e) The HAADF-STEM (d) and ABF-STEM (e) images of the representative SrTiO$_3$/BaTiO$_3$ (4 u.c.)/SrRuO$_3$ (8 u.c.) heterostructures clearly show the atomically sharp interface without any oxygen octahedral tilting. (f) Statistical analysis of depth-dependent oxygen octahedral tilting angles with monolayer resolution shows no oxygen octahedral tilting across the entire thin films.

$H = H^{\text{hop}} + H^{\text{soc}} + H^R$ incorporating Ru $t_{2g}$ orbitals based on first principles calculations. $H^{\text{hop}}$, $H^{\text{soc}}$ and $H^R$ correspond to the hopping term, the atomic-like spin–orbit interaction and the Rashba interaction respectively. A rigid exchange spin splitting is introduced to the hopping term, and its value is determined by the measured magnetization. The Rashba interaction arising from the application of the perpendicular electric field results

in the change of electrons orbital characters in hopping processes [55–57]. The strength of the Rashba interaction is represented by $\lambda$ (see supplementary data section 15 for details on calculation).

In the continuum limit, the energy of the 2D system is a functional of the magnetization field through both exchange interaction $\boldsymbol{J}$ and the DM interaction $\boldsymbol{D}$,
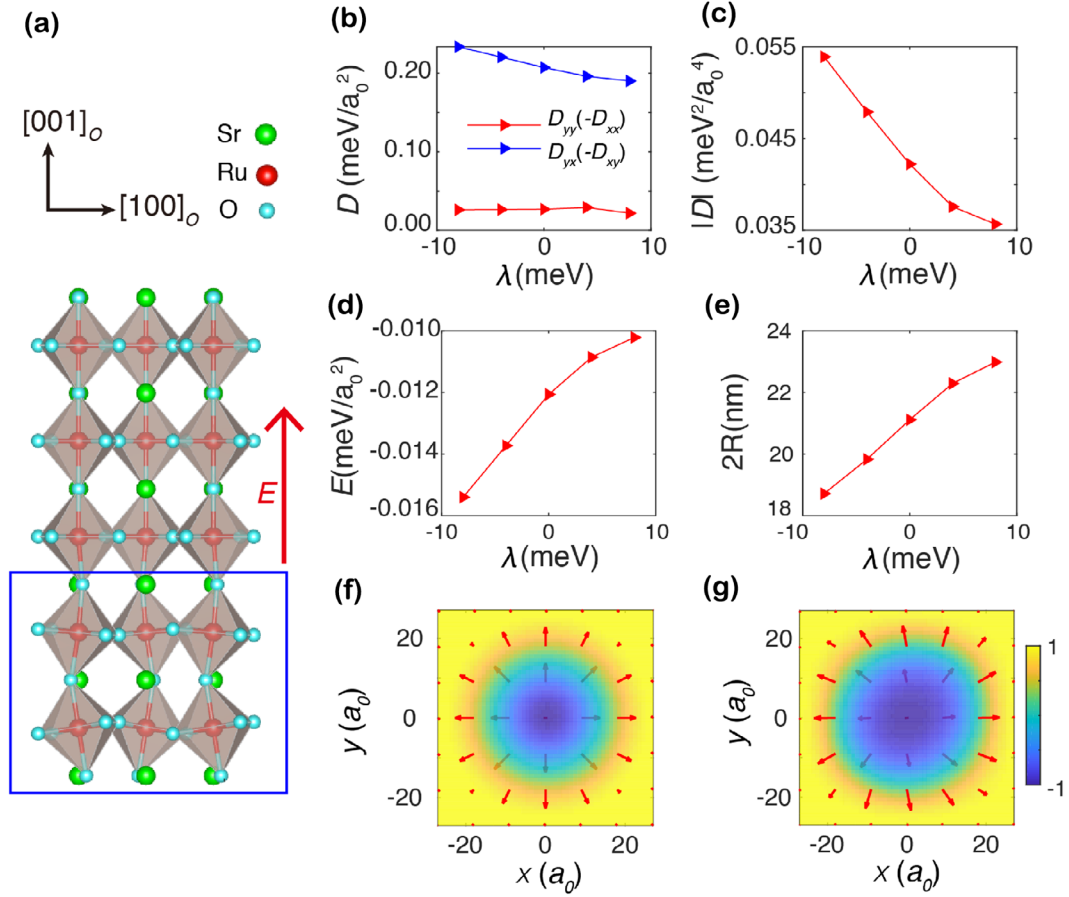
**Figure 5.** Calculated DM interaction and skyrmion configuration. (a) Schematic view of structure model of SrRuO$_3$ slab used in the calculations. (b) Electric-field dependence of DM interaction coefficients for the 5 u.c.-thick SrRuO$_3$ slab. $\lambda$ represents the strength of Rashba interaction, which is approximately proportional to the strength of electric-field magnitude. (c) Electric-field dependence of determinant $|D| = D_{xx}D_{yy} - D_{xy}D_{yx}$ for DM interaction. (d) Minimized energy density under different electric-field strengths. (e) Skyrmion diameter determined by minimizing energy density. (f) and (g) Calculated structures of skyrmion with the general form (f) and with fully relaxed (g) in a square grid. The arrows indicate the in-plane components of the spins, and the colors represent the out-of-plane component.

$$E = \frac{1}{S} \int dr J (\nabla \boldsymbol{m})^2 + \sum_{\mu} \boldsymbol{D}_{\mu} \cdot (\partial_{\mu} \boldsymbol{m} \times \boldsymbol{m}), \qquad (3)$$

where $\boldsymbol{m}$ is the magnetization direction at $\boldsymbol{r}$, $S$ is the integral area, and vector $\boldsymbol{D}_{\mu}$ parametrizes effective DM interaction with $\mu = x, y, z$. The strength of $J = 0.71 \, \text{meV}/a_0$ is obtained according to the measured $M–T$ relation, where $a_0$ is the nearest Ru–Ru distance (see figure S14 in supplementary data). The coefficients of DM interaction $\boldsymbol{D}_{\mu}$ are calculated from the spin susceptibility based on the tight-binding model (see supplementary data in sections 14 and 15 for details on calculation) [58]. The structure of an isolated skyrmion can be obtained by minimizing the energy in equation (3) (see supplementary data in section 16 for details on calculation) [19, 24], while the optimal diameter of the skyrmion corresponds to the unit cell size of the magnetic configuration.

We first examine the effects of SrTiO$_3$ substrate and the interfacial oxygen octahedral tilting induced by structural phase transition. The SrTiO$_3$ substrate induces on-site energy difference about 31 meV between the $d_{zx}$ ($d_{yz}$) orbitals of first layer Ru atoms and the second layer Ru atoms close to the substrate, based on our density-functional theoretic calculations. The calculated nonzero components of DM interaction for SrRuO$_3$ film with tetragonal structure are $D_{xy} = -D_{yx} = 0.052 \, \text{meV}/a_0^2$, in the absence of oxygen octahedral tilting and the external perpendicular electric field. The diameter of isolated skyrmions, upon energy minization, is around 84 nm, which is much larger than the estimated value (8–30 nm) from the experimentally measured THE. Therefore, the observed THE cannot be attributed entirely to the SrTiO$_3$/ SrRuO$_3$ interface effect, and seem to be enhanced by additional DM interaction. Indeed, such enhancement comes from the interfacial oxygen octahedral tilting induced by local orthorhombic-to-tetragonal structural phase transition of SrRuO$_3$ (figure 3).

The local orthorhombic-to-tetragonal phase transition is presented in the SrRuO$_3$ film as shown in figure 5(a), where the oxygen octahedral tilting of the first and second SrRuO$_3$ layer close to SrTiO$_3$ substrate highlighted by a blue rectangular box. According to the STEM measurement (see figure S9 in Supplementary data), the tilting angles are about 4° for the first layer SrRuO$_3$ and 2° for the second layer SrRuO$_3$. When these seemingly minute structural modulations are considered in the tight-binding model, the computed DM interaction is shown in figures 5(b) and (c) ($\lambda = 0$ case). The obtained skyrmion configuration is Néel-type [19, 24] with a diameter of 22 nm

(figure 5(f)), comparable with the experimental estimate. Therefore, the interfacial oxygen octahedral tilting induced by local structural phase transition plays a critical role in the formation of skyrmion and the observed THE. Starting with the optimal continuum magnetization field, we further relax the skyrmion structure over a square grid with fixed boundary to minimize the energy density using conjugate-gradient method. The computed configuration of Néel-type skyrmion (figure 5(g)) remains essentially unchanged.

Finally, the electric-field control of THE is numerically simulated in the presence of interfacial oxygen octahedral tilting. The strength of electric field is approximately proportional to the Rashba interaction strength $\lambda$. Figures 5(b) and (c) display the numerical results of DM interaction as functions of $\lambda$, showing that the components of DM interaction are remarkably sensitive to the variation $\lambda$. The determinant $|D| = D_{xx}D_{yy} - D_{xy}D_{yx}$ is always positive, indicating that the system favors to form skyrmions rather than antiskyrmions [59], over the range of electric field considered. The energy minima of skyrmion and the skyrmion size as a function of $\lambda$ are presented in figures 5(d) and (e), respectively. As $\lambda$ changes from negative to positive, the energy density becomes higher and the size of skyrmion turns out to be larger. This is in good agreement with the experimental measurements of THE, which gives larger size of skyrmion at positive gate voltages. The perpendicular electric field at the ultrathin SrTiO$_3$/SrRuO$_3$ interface further breaks the inversion symmetry causing Rashba interaction, which is observed as electrical control of Rashba-type band splitting in an inverted In$_{0.53}$Ga$_{0.47}$As/In$_{0.52}$Al$_{0.48}$As semiconductor heterostructure [39] and LaAlO$_3$/SrTiO$_3$ oxide interface [60]. This factor leads to a sizeable interface DM interaction modulation and ultimately leads to the observed electric-field induced modulation of THE. Recent work has shown that inhomogeneous magnetoelectric properties can also affect the AHE for ultrathin SrRuO$_3$ films on NdGaO$_3$ substrates [61]. It is difficult to completely rule out the alternative explanation, but the studied system also presents a spatial gradient of octahedral tilting and rotation near film/substrate interface induced by distorted substrate itself which can explain the observed characteristics.

## 4. Conclusions

To summarize, we demonstrate the existence of THE in ultrathin 4D SrRuO$_3$ ($\leqslant 8$ u.c.) films grown on SrTiO$_3$(001) substrates. The THE can be greatly modulated by an electric-field. The physical origin of the THE in SrRuO$_3$ can be understood as follows: A combination of broken inversion symmetry induced by RuO$_6$ octahedral tilting at the SrTiO$_3$/SrRuO$_3$ interface region and strong spin–orbit interaction of SrRuO$_3$ generate chiral DM interaction. It is the DM interaction that stabilizes Néel-type magnetic skyrmion spin texture in SrRuO$_3$ single-layered films. It is known that a spin texture with multi-$q$ spiral can also lead to THE [62]. In our calculations, we have also assayed possible spiral spin textures with a pair of $q$ vectors. Upon energy minimization, these spiral structures lead to a square lattice of skyrmions with identical chirality and similar size as in the single-skyrmion model discussed above. Therefore, our discussion based on the formation energy of single skyrmion provides an adequate model for the system.

The main contributions of the present work are the following: (i) the SrRuO$_3$ single-layered films can generate the THE; (ii) the realization of electric-field control of DM interaction paves an avenue for electrically tuning the chiral spin structures, which has been proposed with potential applications for high-density and low power consumption memories; (iii) oxygen octahedral tilting not only serves as an intrinsic mechanism for the THE in oxides system, but also plays a role to produce and/or modulate DM interaction in oxide films. Such a bridge will connect the oxide community and spintronics, as well as topological materials community to explore more interesting phenomenon based on the oxides. No observation of skyrmions by real-space spin-sensitive imaging techniques (e.g. Lorenz transmission electron microscopy (LTEM)) is likely due to the too small skyrmion size in the SrRuO$_3$ films. Our observation of the THE and its electrical modulation feature would facilitate further studies of the topological skyrmion spin textures in more oxide materials.

## ORCID iDs

Jirong Sun https://orcid.org/0000-0003-1238-8770
Cheng Song https://orcid.org/0000-0002-7651-9031
Wei Liu https://orcid.org/0000-0002-5368-3605
Feng Pan https://orcid.org/0000-0002-3788-7894

## References

[1] Taguchi Y, Oohara Y, Yoshizawa H, Nagaosa N and Tokura Y 2001 Spin chirality, Berry phase, and anomalous Hall effect in a frustrated ferromagnet *Science* **291** 2573–6
[2] Bruno P, Dugaev V K and Taillefumier M 2004 Topological Hall effect and Berry phase in magnetic nanostructures *Phys. Rev. Lett.* **93** 096806

J. Phys. D: Appl. Phys. **52** (2019) 404001

Y Gu *et al*

[3] Onoda M, Tatara G and Nagaosa N 2004 Anomalous Hall effect and skyrmion number in real and momentum spaces *J. Phys. Soc. Japan* **73** 2624–7

[4] Day C 2009 Exotic spin textures show up in diverse materials *Phys. Today* **62** 12–3

[5] Schulz T, Ritz R, Bauer A, Halder M, Wagner M, Franz C, Pfleiderer C, Everschor K, Garst M and Rosch A 2012 Emergent electrodynamics of skyrmions in a chiral Magnet *Nat. Phys.* **8** 301–4

[6] Yu X Z, Kanazawa N, Zhang W Z, Nagai T, Hara T, Kimoto K, Matsui Y, Onose Y and Tokura Y 2012 Skyrmion flow near room temperature in an ultralow current density *Nat. Commun.* **3** 988

[7] Mühlbauer S, Binz B, Jonietz F, Pfleiderer C, Rosch A, Neubauer A, Georgii R and Böni P 2009 Skyrmion lattice in a chiral magnet *Science* **323** 915–9

[8] Yu X Z, Onose Y, Kanazawa N, Park J H, Han J H, Matsui Y, Nagaosa N and Tokura Y 2010 Real-space observation of a two-dimensional skyrmion crystal *Nature* **465** 901–4

[9] Yu X Z, Kanazawa N, Onose Y, Kimoto K, Zhang W Z, Ishiwata S, Matsui Y and Tokura Y 2011 Near room-temperature formation of a skyrmion crystal in thin-films of the helimagnet FeGe *Nat. Mater.* **10** 106–9

[10] Soumyanarayanan A *et al* 2017 Tunable room-temperature magnetic skyrmions in Ir/Fe/Co/Pt multilayers *Nat. Mater.* **16** 898–904

[11] Jiang W, Chen G, Liu K, Zang J, te Velthuis S G E and Hoffmanne A 2017 Skyrmions in magnetic multilayers *Phys. Rep.* **704** 1–49

[12] Yu X, Tokunaga Y, Taguchi Y and Tokura Y 2017 Variation of topology in magnetic bubbles in a colossal magnetoresistive manganite *Adv. Mater.* **29** 1603958

[13] Matsuno J, Ogawa N, Yasuda K, Kagawa F, Koshibae W, Nagaosa N, Tokura Y and Kawasaki M 2016 Interface-driven topological Hall effect in SrRuO₃–SrIrO₃ bilayer *Sci. Adv.* **2** e1600304

[14] Ohuchi Y, Matsuno J, Ogawa N, Kozuka Y, Uchida M, Tokura Y and Kawasaki M 2018 Electric-field control of anomalous and topological Hall effects in oxide bilayer thin films *Nat. Commun.* **9** 213

[15] Meng K-Y *et al* 2019 Observation of nanoscale skyrmions in SrIrO₃/SrRuO₃ bilayers *Nano Lett.* **19** 3169–75

[16] Wang L *et al* 2018 Ferroelectrically tunable magnetic skyrmions in ultrathin oxide heterostructures *Nat. Mater.* **17** 1087–94

[17] Neubauer A, Pfleiderer C, Binz B, Rosch A, Ritz R, Niklowitz P G and Böni P 2009 Topological Hall effect in the a phase of MnSi *Phys. Rev. Lett.* **102** 186602

[18] Nagaosa N and Tokura Y 2013 Topological properties and dynamics of magnetic skyrmions *Nat. Nanotechnol.* **8** 899–911

[19] Yasuda K, Wakatsuki R, Morimoto T, Yoshimi R, Tsukazaki A, Takahashi K S, Ezawa M, Kawasaki M, Nagaosa N and Tokura Y 2016 Geometric Hall effects in topological insulator heterostructures *Nat. Phys.* **12** 555–9

[20] Dzyaloshinsky I 1958 A thermodynamic theory of 'weak' ferromagnetism of antiferromagnetics *J. Phys. Chem. Solids* **4** 241–55

[21] Moriya T 1960 Anisotropic superexchange interaction and weak ferromagnetism *Phys. Rev.* **120** 91–8

[22] Boulle O *et al* 2016 Room-temperature chiral magnetic skyrmions in ultrathin magnetic nanostructures *Nat. Nanotechnol.* **11** 449–54

[23] Zhao D *et al* 2018 Observation of unconventional anomalous Hall effect in epitaxial CrTe thin films *Nano Res.* **11** 3116–21

[24] Liu C, Zang Y, Ruan W, Gong Y, He K, Ma X, Xue Q-K and Wang Y 2017 Dimensional crossover-induced topological Hall effect in a magnetic topological insulator *Phys. Rev. Lett.* **119** 176809

[25] Qin Q, Liu L, Lin W, Shu X, Xie Q, Lim Z, Li C, He S, Chow G M and Chen J 2019 Emergence of topological Hall effect in a SrRuO₃ single layer *Adv. Mater.* **31** 1807008

[26] Lu W, Yang P, Song W D, Chow G M and Chen J S 2013 Control of oxygen octahedral rotations and physical properties in SrRuO₃ films *Phys. Rev.* B **88** 214115

[27] Chang S H, Chang Y J, Jang S Y, Jeong D W, Jung C U, Kim Y-J, Chung J-S and Noh T W 2011 Thickness-dependent structural phase transition of strained SrRuO₃ ultrathin films: the role of octahedral tilt *Phys. Rev.* B **84** 104101

[28] He J, Borisevich A, Kalinin S V, Pennycook S J and Pantelides S T 2010 Control of octahedral tilts and magnetic properties of perovskite oxide heterostructures by substrate symmetry *Phys. Rev. Lett.* **105** 227203

[29] Liao Z *et al* 2016 Controlled lateral anisotropy in correlated manganite heterostructures by interface-engineered oxygen octahedral coupling *Nat. Mater.* **15** 425–31

[30] Kan D, Aso R, Sato R, Haruta M, Kurata H and Shimakawa Y 2016 Tuning magnetic anisotropy by interfacially engineering the oxygen coordination environment in a transition metal oxide *Nat. Mater.* **15** 432–7

[31] Yi D *et al* 2017 Tuning perpendicular magnetic anisotropy by oxygen octahedral rotations in (La$_{1-x}$Sr$_x$MnO₃)/(SrIrO₃) superlattices *Phys. Rev. Lett.* **119** 077201

[32] Zhang J *et al* 2018 Symmetry mismatch-driven perpendicular magnetic anisotropy for perovskite/brownmillerite heterostructures *Nat. Commun.* **9** 1923

[33] Li F, Song C, Wang Y Y, Cui B, Mao H J, Peng J J, Li S N, Wang G Y and Pan F 2015 Tilt engineering of exchange coupling at *G*-type SrMnO₃/(La,Sr)MnO₃ interfaces *Sci. Rep.* **5** 16187

[34] Koster G, Klein L, Siemons W, Rijnders G, Dodge J S, Eom C-B, Blank D H A and Beasley M R 2012 Structure, physical properties, and applications of SrRuO₃ thin films *Rev. Mod. Phys.* **84** 253–98

[35] Fang Z, Nagaosa N, Takahashi K S, Asamitsu A, Mathieu R, Ogasawara T, Yamada H, Kawasaki M, Tokura Y and Terakura K 2003 The anomalous Hall effect and magnetic monopoles in momentum space *Science* **302** 92–5

[36] Itoh S, Endoh Y, Yokoo T, Ibuka S, Park J-G, Kaneko Y, Takahashi K S, Tokura Y and Nagaosa N 2016 Weyl fermions and spin dynamics of metallic ferromagnet SrRuO₃ *Nat. Commun.* **7** 11788

[37] Si L, Janson O, Li G, Zhong Z, Liao Z, Koster G and Held K 2017 Quantum anomalous Hall state in ferromagnetic SrRuO₃ (1 1 1) bilayers *Phys. Rev. Lett.* **119** 026402

[38] Song C, Cui B, Li F, Zhou X and Pan F 2017 Recent progress in voltage control of magnetism: materials, mechanisms, and performance *Prog. Mater. Sci.* **87** 33–82

[39] Nitta J, Akazaki T, Takayanagi H and Enoki T 1997 Gate control of spin–orbit interaction in an inverted In$_{0.53}$Ga$_{0.47}$As/In$_{0.52}$Al$_{0.48}$As heterostructure *Phys. Rev. Lett.* **78** 1335–8

[40] Srivastava T *et al* 2018 Large-voltage tuning of Dzyaloshinskii–Moriya interaction: a route towards dynamic control of skyrmion chirality *Nano Lett.* **18** 4871–7

[41] Toyota D *et al* 2005 Thickness-dependent electronic structure of ultrathin SrRuO₃ films studied by *in situ* photoemission spectroscopy *Appl. Phys. Lett.* **87** 162508

[42] Xia J, Siemons W, Koster G, Beasley M R and Kapitulnik A 2009 Critical thickness for itinerant ferromagnetism in ultrathin films of SrRuO₃ *Phys. Rev.* B **79** 140407

[43] Shimizu S, Takahashi K S, Kubota M, Kawasaki M, Tokura Y and Iwasa Y 2014 Gate tuning of anomalous Hall effect in ferromagnetic metal SrRuO₃ *Appl. Phys. Lett.* **105** 163509

J. Phys. D: Appl. Phys. **52** (2019) 404001

Y Gu *et al*

[44] Mathieu R, Asamitsu A, Yamada H, Takahashi K S, Kawasaki M, Fang Z, Nagaosa N and Tokura Y 2004 Scaling of the anomalous Hall effect in $Sr_{1-x}Ca_xRuO_3$ *Phys. Rev. Lett.* **93** 016602

[45] Worledge D C and Geballe T H 2000 Negative spin-polarization of $SrRuO_3$ *Phys. Rev. Lett.* **85** 5182–5

[46] Nadgorny B, Osofsky M S, Singh D J, Woods G T, Soulen R J, Lee M K, Bu S D and Eom C B 2003 Measurements of spin polarization of epitaxial $SrRuO_3$ thin films *Appl. Phys. Lett.* **82** 427

[47] Müller K A and Burkard H 1979 $SrTiO_3$: an intrinsic quantum paraelectric below 4 K *Phys. Rev.* B **19** 3593–602

[48] Mizuno H, Yamada K T, Kan D, Moriyama T, Shimakawa Y and Ono T 2017 Electric-field-induced modulation of the anomalous Hall effect in a heterostructured itinerant ferromagnet $SrRuO_3$ *Phys. Rev.* B **96** 214422

[49] Thomas S *et al* 2017 Localized control of Curie temperature in perovskite oxide film by capping-layer-induced octahedral distortion *Phys. Rev. Lett.* **119** 177203

[50] Qiao L *et al* 2015 Dimensionality controlled octahedral symmetry-mismatch and functionalities in epitaxial $LaCoO_3/SrTiO_3$ heterostructures *Nano Lett.* **15** 4677–84

[51] Moon E J, Balachandran P V, Kirby B J, Keavney D J, Sichel-Tissot R J, Schlepütz C M, Karapetrova E, Cheng X M, Rondinelli J M and May S J 2014 Effect of interfacial octahedral behavior in ultrathin manganite films *Nano Lett.* **14** 2509–14

[52] Kan D, Aso R, Kurata H and Shimakawa Y 2015 Research update: interface-engineered oxygen octahedral tilts in perovskite oxide heterostructures *APL Mater.* **3** 062302

[53] Aso R, Kan D, Shimakawa Y and Kurata H 2014 Octahedral tilt propagation controlled by A-site cation size at perovskite oxide heterointerfaces *Cryst. Growth Des.* **14** 2128–32

[54] Fert A, Cros V and Sampaio J 2013 Skyrmions on the track *Nat. Nanotechnol.* **8** 152–6

[55] Chen Y, Bergman D L and Burkov A A 2013 Weyl fermions and the anomalous Hall effect in metallic ferromagnets *Phys. Rev.* B **88** 125110

[56] Khalsa G, Lee B and MacDonald A H 2013 Theory of $t_{2g}$ electron–gas Rashba interactions *Phys. Rev.* B **88** 041302

[57] Zhong Z, Tóth A and Held K 2013 Theory of spin-orbit coupling at $LaAlO_3/SrTiO_3$ interfaces and $SrTiO_3$ surfaces *Phys. Rev.* B **87** 161102

[58] Koretsune T, Kikuchi T and Arita R 2018 First-principles evaluation of the Dzyaloshinskii–Moriya interaction *J. Phys. Soc. Jaapn* **87** 041011

[59] Hoffmann M, Zimmermann B, Müller G P, Schürhoff D, Kiselev N S, Melcher C and Blügel S 2017 Antiskyrmions stabilized at interfaces by anisotropic Dzyaloshinskii–Moriya interactions *Nat. Commun.* **8** 308

[60] Caviglia A D, Gabay M, Gariglio S, Reyren N, Cancellieri C and Triscone J-M 2010 Tunable Rashba spin-orbit interaction at oxide interfaces *Phys. Rev. Lett.* **104** 126803

[61] Kan D, Moriyama T, Kobayashi K and Shimakawa Y 2018 Alternative to the topological interpretation of the transverse resistivity anomalies in $SrRuO_3$ *Phys. Rev.* B **98** 180408

[62] Binz B and Vishwanath A 2008 Chirality induced anomalous-Hall effect in helical spin crystals *Physica* B **403** 1336–40